

# A Code-Domain, In-Band, Full-Duplex Wireless Communication Link With Greater Than 100-dB Rejection

Ahmed Hamza<sup>ID</sup>, *Graduate Student Member, IEEE*, Aravind Nagulu<sup>ID</sup>, *Member, IEEE*,  
 Alfred Festus Davidson<sup>ID</sup>, *Graduate Student Member, IEEE*, Jonathan Tao, *Student Member, IEEE*,  
 Cameron Hill<sup>ID</sup>, *Member, IEEE*, Hussam AlShammary<sup>ID</sup>, *Member, IEEE*,  
 Harish Krishnaswamy<sup>ID</sup>, *Member, IEEE*, and James Buckwalter<sup>ID</sup>, *Senior Member, IEEE*

**Abstract**—This article presents a CMOS-based, code-domain (CD), full-duplex (FD) transceiver operating in a link at 1 GHz. The CD FD link rejects in-band transmitter self-interference (TX SI) by more than 100 dB through a combination of pseudo-noise (PN) code orthogonality, circulator, and digital cancellation algorithms. A nonmagnetic CMOS circulator based on switched transmission lines is used as an antenna interface with >40-dB maximum rejection. Then, transmitter (TX) and receiver (RX) modulators spread the TX SI and correlate the desired RX signal in the RF domain. Orthogonality between the PN codes allows an additional >40-dB maximum rejection relaxing the FD transceiver linearity requirements. Finally, digital self-interference cancellation (SIC) eliminates any residual TX SI in the digital domain using a least mean squares (LMS) estimation for the SI channel based on a nonlinear truncated Volterra series model. The digital SIC can have almost 40 dB of rejection depending on the SI power level. An implemented FD node leverages these techniques to achieve an overall rejection that is around 104 dB bringing the TX signal from 20 dBm to the noise floor of the RX at -85 dBm.

**Index Terms**—Cancellation, circulator, CMOS, code-division multiple access (CDMA), code domain, full duplex (FD), pseudo-noise (PN) sequence, self-interference, simultaneous transmit and receive (STAR).

## I. INTRODUCTION

FULL-DUPLEX (FD) communication requires the receiver (RX) to operate simultaneously at the same frequency channel as the transmitter (TX) [1]–[3]. FD offers enhanced bandwidth (BW) efficiency (nearly 2×) along with

Manuscript received July 21, 2020; revised September 16, 2020; accepted October 6, 2020. Date of publication November 11, 2020; date of current version January 5, 2021. This work was supported by the DARPA SPAR Program under Grant HR0011-17-2-0003. This article is an expanded version from the 2020 IEEE MTT-S International Microwave Symposium, Los Angeles, CA, USA, August 4–6, 2020 (*Corresponding author: Ahmed Hamza*.)

Ahmed Hamza, Jonathan Tao, Cameron Hill, Hussam AlShammary, and James Buckwalter are with the Department of Electrical and Computer Engineering, University of California at Santa Barbara, Santa Barbara, CA 93106 USA (e-mail: ahsayed@ucsb.edu).

Aravind Nagulu, Alfred Festus Davidson, and Harish Krishnaswamy are with the Department of Electrical Engineering, Columbia University, New York, NY 10027 USA (e-mail: harish@ee.columbia.edu).

Color versions of one or more of the figures in this article are available online at <https://ieeexplore.ieee.org>.

Digital Object Identifier 10.1109/TMTT.2020.3035354

other benefits in upper network layer, such as the medium access control (MAC) layer [1], [4].

One of the main challenges in FD communication is addressing the huge dynamic range (DR) difference between the TX and RX signal powers that can reach more than 110 dB. Prior work has addressed this problem through a variety of rejection and cancellation techniques, as shown in Fig. 1. These techniques can be categorized into antenna domain, RF domain, analog (or baseband domain), and digital cancellation.

Antenna-based techniques achieve rejection through isolation at the antenna interface. Prior work has exhibited using two or more antennas with spatial separation, orthogonally polarized antennas, antenna arrays, or a relay antenna with wavetraps [4]–[12]. One of the main challenges in these techniques is the form factor of the FD transceiver. Multiple antennas occupy a large area overhead given the required antenna separation making them unsuitable for mobile devices. Otherwise, magnetic circulators [13]–[17], electrically balanced duplexers (EBDs) [18], [19], or compact CMOS circulators [20] can be used in a single antenna FD transceiver. An EBD reduces the FD transceiver form factor at the expense of at least 3-dB TX power loss penalty reducing the TX efficiency. The 3-dB TX power loss penalty can be overcome by using a circulator instead of the EBD. Magnetic circulators occupy large area making nonmagnetic CMOS circulators the most feasible option for compact FD transceivers [21], [22].

RF rejection operates by injecting a replica TX signal to the RX and canceling it at the low-noise amplifier (LNA) [7], [9], [10], [13], [15], [16], [20]. RF cancellers use tunable delays or phase shifters and tunable gain elements to emulate the SI channel response between the TX and the RX in a time-domain [23] or frequency-domain approach [24]. Analog cancellation operates in the baseband section after frequency downconversion by the mixer and is effective when the SI does not generate significant in-band (IB) distortion [25], [26]. Emulating the SI channel between the TX and the RX with high accuracy is one of the main challenges in high-rejection RF/analog cancellers. The SI channel is characterized by having large delay spreads due to multipath and environmental

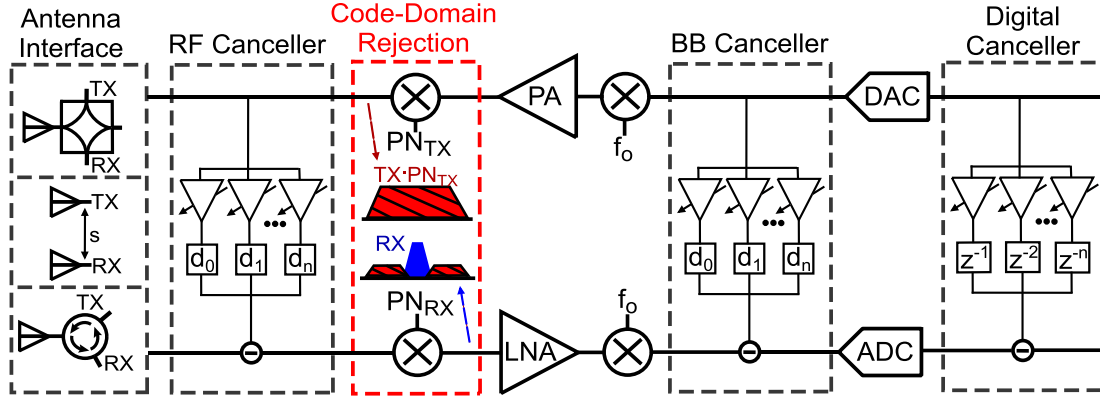


Fig. 1. Different TX SI rejection techniques in FD transceivers, including antenna interface rejection, RF cancellation, the proposed CD rejection, baseband cancellation, and digital cancellation. A combination of these techniques can be used to achieve the required rejection.

reflections. A high-rejection time-domain canceller requires long delay lines with small delay resolution to achieve a good approximation of the SI channel, which is challenging and ultimately results in noncompact designs that are not compatible with CMOS integration. Moreover, the SI channel is dynamic requiring adaptive RF filters for frequency-domain cancellers increasing their design challenges and power/area overhead.

Digital self-interference cancellation (SIC) exploits the computational-scaling available from CMOS and operates by estimating the SI channel using digital signal processing (DSP) to cancel the residual transmitter self-interference (TX SI) to the RX noise floor [7], [11]–[17], [20]. Employing a nonlinear channel estimation algorithm in the digital domain cancels the IB distortion along with the fundamental TX SI.

The different FD techniques are summarized in Fig. 1, and a comprehensive survey of these techniques can be found in [3]. This article presents a code-domain (CD) FD transceiver that employs the orthogonality between pseudo-noise (PN) codes to reject the TX signal at the RF domain. The proposed FD transceiver uses a nonmagnetic CMOS circulator for a compact form factor and digital SIC to increase the overall TX rejection along with the RF CD rejection. RF CD rejection overcomes some of the challenges of previous SIC techniques as PN codes are resilient to the SI channel multipath propagation effects due to the PN code orthogonality for any lag and they can be implemented with a pair of TX and RX modulators using high-linearity CMOS RF switches allowing small-form-factor FD transceivers with minimal power overhead. It is also worth mentioning that spreading the RF spectrum with PN codes is advantageous with respect to the required circulator linearity allowing higher TX power levels compared to the prior art.

CMOS circulators and CD rejection techniques were previously proposed in [27] and [28], respectively, which focused on the stand-alone implementation of each subsystem. This article expands on these papers and on an earlier conference paper at the 2020 International Microwave Symposium (IMS 2020) [29] to present a detailed discussion about the proposed CD FD transceiver. This article highlights the challenges in implementing a full system and how system-level integration

and the accompanied nonidealities affect the rejection of each subsystem when they coexist. Measurements were used to quantify the effects of system-level integration, and solutions were proposed to overcome some of these challenges. Section II discusses the proposed FD transceiver implementation with details about the nonmagnetic circulator, TX and RX modulators, and digital cancellation algorithm performance. Section III addresses the challenges in achieving the RF CD operation and proposes solutions to overcome these challenges. Section IV outlines some of the unique advantages of RF CD signal processing, such as linearity improvement, and blocker/multipath tolerance in practical wireless environments. Section V presents the measurement results of the proposed CD FD transceiver.

## II. PROPOSED CD FD TRANSCEIVER

The proposed CD FD transceiver is shown in Fig. 2 and is built upon a software-defined radio (SDR) that allows reconfiguration of the radio parameters, such as the carrier frequency, data rate, modulation characteristics, and TX power. A National Instruments universal software radio peripheral (NI USRP 2930) [30] is used as an SDR and controlled through Labview and MATLAB. Using an SDR allows a fair evaluation of the proposed system given the limited resources of a real transceiver [such as analog-to-digital converter (ADC) sampling rate and resolution, and RX noise figure (NF)] compared to using high-end, off-the-shelf measurement equipment, such as oscilloscopes and spectrum analyzers. The USRP provides access to the TX and RX RF data along with the BB IQ data streams that are used for digital SIC.

The USRP is preceded by the proposed high-rejection RF interface consisting of the TX and RX code modulators and the CMOS circulator. More details about the modulators and circulators are presented in Sections II-B and II-C. Finally, a commercial-off-the-shelf (COTS) antenna is used to evaluate the effect of antenna voltage standing wave ratio (VSWR) on the achieved rejection. A dual-band, omnidirectional antenna (VERT900 antenna) covering 824–960- and 1710–1990-MHz frequency range is used [31] as a demonstrative example.

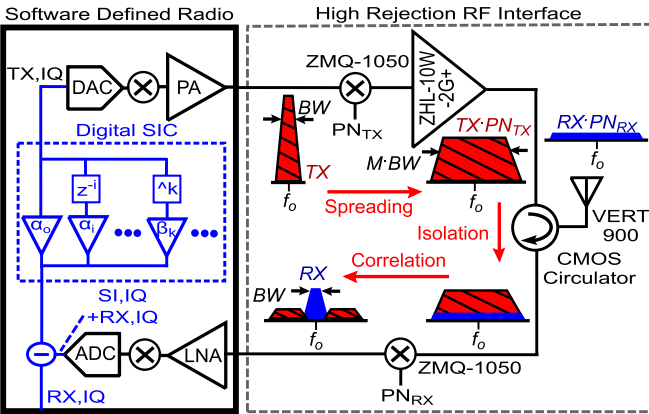


Fig. 2. Proposed CD FD transceiver employing a nonmagnetic CMOS circulator, TX/RX code modulators at RF, and digital SIC.

### A. FD Transceiver Requirements

Implementing an FD transceiver with high SI rejection requires careful consideration of the specifications of the various subblocks of the transceiver. Also, targeting a TX power of  $>20$  dBm increases the linearity, compression, and rejection requirements of the RF interface. An FD link analysis is presented for the proposed CD FD transceiver relating the specifications of various blocks and how they impact the performance of the proposed transceiver.

The antenna interface greatly impacts the performance of subsequent RX blocks. Circulators are the optimum choice for FD systems allowing compact FD systems with a single antenna while avoiding the fundamental 3-dB loss of the EBD. Magnetic circulators offer  $\sim 15$  dB of isolation [32] requiring the RX modulator to handle  $>5$ -dBm TX-SI to target  $>20$ -dBm TX power level, which is challenging. This leaves nonmagnetic CMOS circulators with  $>40$  dB of isolation and watt-level power handling as the only currently viable option for the proposed CD FD transceiver [33], [34]. CMOS circulators greatly relax the RX modulators' power-handling requirement to  $-20$  dBm. However, this comes with an extra challenge for the circulator linearity requirements.

The circulator should be highly linear such that any third-order intermodulation (IM3) tones are below the minimum detectable signal (MDS) of the RX. The MDS of the RX is given by

$$\text{MDS} = -174 + 10 \times \log_{10}(\text{BW}) + \text{NF} \quad (1)$$

where NF is the noise figure of the RX. The NF of the implemented RX includes the noise from the USRP, circulator, and PN modulators. The USRP has an average NF of 6 dB [30], the circulator has 2.5 dB NF [34], the modulator NF is 5 dB consistent with its IL [35], and extra 2.5 dB are added to the NF to account for extra losses from used cables, baluns, and connectors. This results in an overall NF of 16 dB for the RX and an MDS of  $-88$  dBm for a sampling BW of 10 MHz.<sup>1</sup>

<sup>1</sup>The sampling BW is the used chip rate to avoid aliasing. The NF can be reduced by  $\sim 5$ dB for a fully integrated RX by reducing the modulators and connectors' losses.

The required circulator IIP3 is given by [20], [36]

$$\text{IIP3}_{\text{circ}} = \frac{3 \times P_{\text{TX}} - \text{Rej}_{\text{circ}} - \text{Rej}_{\text{dig}} - P_{\text{RX,IM3}}}{2} \quad (2)$$

where  $P_{\text{RX,IM3}}$  is the IM3 power level at the RX due to circulator nonlinearity and should be reduced to the MDS signal level. This results in a circulator TX–RX IIP3 requirement of 34 dBm to handle a 20-dBm TX signal, assuming that 40 dB of rejection is achieved from each of the circulator and nonlinear digital cancellation.<sup>2</sup> A similar analysis shows that the modulator linearity requirement is not a limitation, given that the RX modulator handles a TX SI of  $-20$  dBm due to the available 40 dB of rejection from the circulator.

The above analysis also indicates that 108 dB of rejection is required for the FD transceiver to bring the 20-dBm TX signal to the noise floor of the RX at  $-88$  dBm. This rejection is budgeted among the three used domains such that  $\sim 40$  dB of rejection is achieved from the circulator, another  $\sim 40$  dB from CD rejection, and the remaining rejection from digital SIC. The actual performance of the FD transceiver slightly deviates from the theoretically calculated values due to various system imperfections, as discussed in Section V.

### B. TX and RX Modulators

The TX signal is spread by a PN code ( $\text{PN}_{\text{TX}}$ ), whereas the RX signal is correlated by an orthogonal PN code ( $\text{PN}_{\text{RX}}$ ). Both codes are clocked at a chip rate that is  $M$  times the symbol rate, where  $M$  is the length of the PN code. The TX signal spreads across a BW  $\text{BW}_{\text{spread}}$  that is  $M$  times the signal BW,  $\text{BW}_{\text{sig}}$ . Spreading RF signals at high chip rates requires high-speed modulators.

Minicircuits ZMQ-1050 modulators were used to spread and correlate the TX and RX signals [35]. COTS modulators allow easier experimentation of the FD node and comparison of code parameters. CMOS CD FD implementations for the RX correlators were presented in [37] and [38] allowing  $<3$ -dB IL and  $>10$ -dBm compression point and post-power amplifier (PA). TX modulators were presented in [39] and [40] with  $<1.5$ -dB IL and  $>30$ -dBm power-handling capability. Consequently, there is no limitation in implementing a compact CMOS CD FD RF front end, including the TX and RX modulators along with the CMOS circulator.

The modulators operate between 0.8 and 1.05 GHz with an IL of 4.9 dB and a 1-dB compression point of 4 dBm. The modulators support frequencies (chip rates) up to 100 MChip/s and Fig. 3 plots how the IL changes with modulation frequency indicating  $<1$ -dB degradation in IL at very high modulation frequencies. The 4-dBm compression point allows the RX to support TX SI power levels up to 30 dBm, given that the circulator provides  $>30$ -dB rejection. However, the 4-dBm compression point limits the TX power levels. Thus, the TX modulator is followed by a wideband (WB) PA (ZHL-10W-2G+) to allow 30-dBm TX power levels [41].

<sup>2</sup>Assume that code rejection only affects the TX signal and does not reject the IM3 tones generated by the circulator. It will be shown later that spreading improves the circulator IIP3 by PN code processing gain (PG).

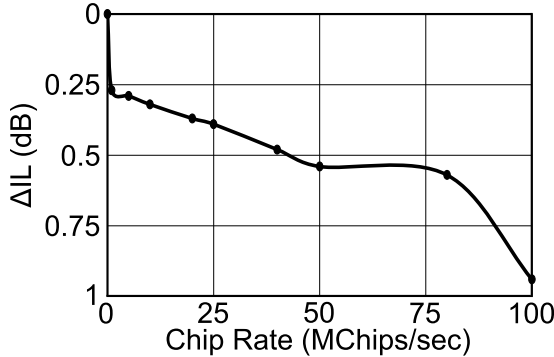


Fig. 3. Measured IL of the TX/RX modulators as a function of chip rate.

### C. Nonmagnetic CMOS Circulator

The circuit implementation of the magnetic-less CMOS circulator is shown in Fig. 4(a) and is based on switched transmission lines. The circulator includes a built-in antenna balancing scheme with tunable feed capacitors at orthogonal feed points to cancel the TX–RX leakage generated due to ANT mismatches and other nonidealities. In addition, a novel clock boosting technique using level-shifted capacitors was used to increase the peak-to-peak voltage of the modulation signal to  $3 \times V_{dd}$  without compromising the long-term reliability of the transistors. The level-shifted capacitors allow the clock path to operate at its regular supply voltage  $V_{dd}$  yet providing a  $3 \times$  modulation signal swing. The circulator consumes  $4 \times$  lower power consumption than the circulator in [33] yet provides  $2.5 \times$  higher power handling at the TX port.

The 1-GHz, 180-nm SOI CMOS circulator exhibits 2.1-/2.6-dB TX-ANT/ANT-RX IL with a 1-dB BW of 172 MHz. When terminated with a  $50\Omega$  termination, the measured TX-to-RX isolation is  $>40$  dB. The feed capacitors can be tuned to achieve  $>40$ -dB isolation across the entire 2.33:1 antenna VSWR and beyond. The circulator achieves TX-ANT and ANT-RX IIP3s of +50 and +36.3 dBm, respectively. The TX-ANT IIP3 is larger than the ANT-RX IIP3 due to the placement of the gyrator next to the RX port, consequently eliminating the TX swing on gyrator switches [27]. The measured TX-ANT  $P_{1dB}$  is +34 dBm, due to the linearity enhancement techniques such as clock boosting and programmable capacitors with device stacking. This large-signal performance represents a significant improvement compared with the prior CMOS circulators [27], [33]. More details about the circulator operation and performance can be found in [34]. The measured TX–RX rejection of the circulator is shown in Fig. 4(b) when a  $50\Omega$  termination and a COTS antenna are connected at the antenna port. The implications of the antenna VSWR on the overall rejection and code orthogonality in terms of group delay (GD) are discussed in Section V.

### D. Digital SIC

Digital SIC was applied to the captured baseband IQ data from the USRP in MATLAB. Digital SIC was implemented with a reduced-order nonlinear Volterra series model for the SI

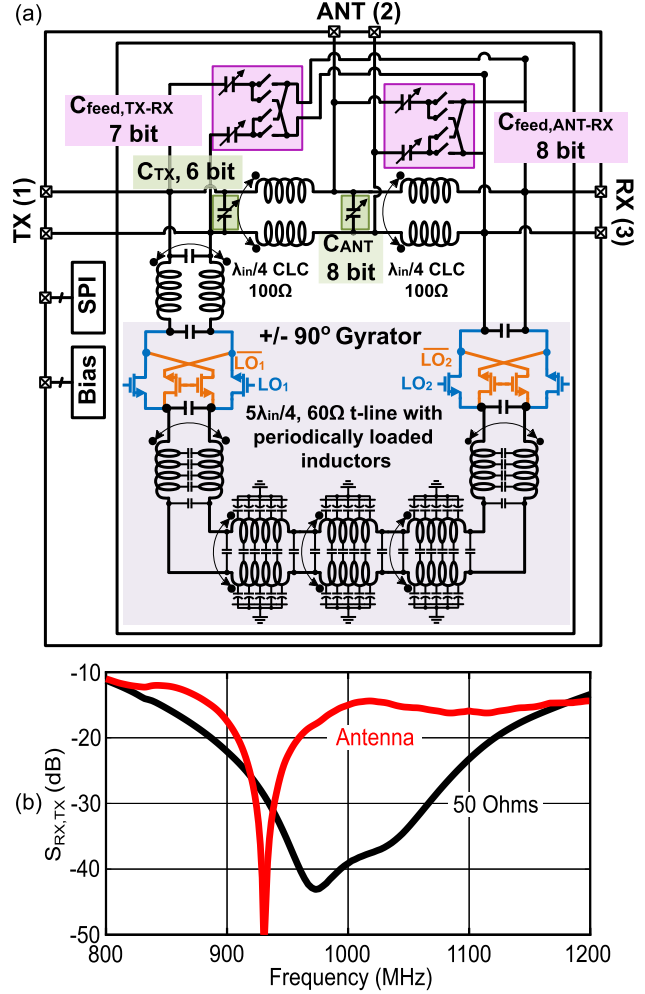


Fig. 4. Multiwatt 1-GHz CMOS circulator employing the concept of switched transmission lines. (a) Circuit schematics. (b) Measured TX–RX rejection with  $50\Omega$  and antenna termination.

channel with least mean squares (LMS) estimation to cancel residual IB SI to the noise floor of the USRP [13]. The model of the digital SIC is

$$SI[n] = \sum_{i=-5}^7 \alpha_i \times TX[n-i] + \sum_{k=3,5,7} \beta_k \times TX^k[n] \quad (3)$$

where  $\alpha$  and  $\beta$  are the coefficients of the linear and nonlinear taps solved by the LMS algorithm.

Fig. 5(a) shows the effect of applying digital SIC at different SI power levels for a 0.625-MSymbol/s QPSK signal sampled at 12.5 MSample/s. Digital SIC increases almost linearly with SI power for SI power levels between  $-75$  and  $-50$  dBm indicating the ability to reduce the SI to the noise level of the USRP. However, the digital SIC deviated from the linear behavior at high SI power levels by compression (SI greater than the ADC DR) and at extremely low SI power levels as the noise floor is approached. This suggests that the SI power should be reduced by the circulator and code rejection to the linear region of the digital SIC for optimal overall SI rejection.

Fig. 5(b) shows the achieved digital SIC at various symbol rates at a fixed ADC sampling rate of 12.5 MSample/s. Digital

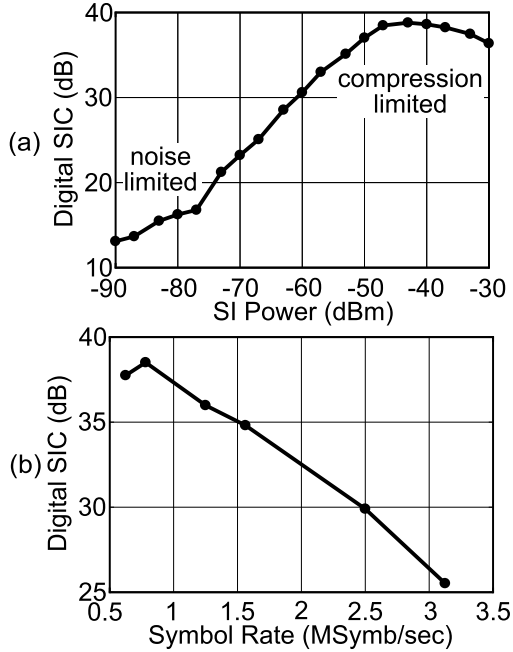


Fig. 5. Digital SIC. (a) Digital SIC versus SI power level. (b) Digital SIC versus symbol rate at a fixed ADC sampling rate.

SIC is reduced as the symbol rate increases due to the reduced number of samples per symbol, which degrades the quality of the SI channel estimation. Fig. 5(b) shows that eight samples per each TX symbol are required to have a rejection  $>35$  dB. It is worth mentioning that this is a hardware limitation and higher symbol rates could be achieved using other high-end reconfigurable transceivers such as [11] and [42], which could possibly allow data rates up to 15 MSymbol/s. However, this requires a spreading BW in excess of 100 MHz, which could be achieved in a two-antenna transceiver configuration to avoid circulator BW limitations.

### III. CHALLENGES OF CD FD

Performing the CD signal processing in the RF domain entails addressing challenges for radio operation in a practical wireless environment. This section explores some of the challenges encountered in designing CD FD transceivers and proposes solutions to overcome these challenges. Meanwhile, numerous advantages are also gained by the RF CD processing that enhances the radio operation. These advantages are subsequently covered in Section IV and verified by measurements.

#### A. Synchronization

CD operation demands the synchronization between at least two transceivers for proper operation. Doing the code correlation in the RF domain adds to the synchronization complexity compared to previous code-division multiple access (CDMA) systems that relied on DSP for code correlation. In CDMA systems, the spread BW is captured by the ADC, which allows utilizing digital resources for code synchronization and correlation. However, by doing the code correlation at the RF

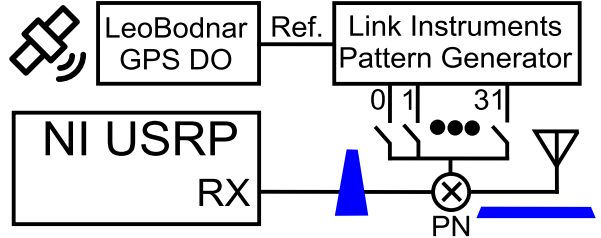


Fig. 6. Synchronization setup using GPSDO.

front end, the RX BB processor will not be able to receive the desired signal unless exact code alignment is guaranteed at the RF correlators.

There are multiple challenges in CD FD transceivers synchronization. First, any two frequency references suffer from an inevitable frequency drift due to temperature, process, and supply variations. This drift complicates the synchronization process and demands using frequency sources with high-frequency stability. Advances in RFIC technologies make GPS available in most cellular devices with low-power and area overheads. These GPS-synchronized RXs can be utilized to provide a stable frequency source [43]. While GPS synchronization is suitable for outdoor environments such as base stations where a reliable GPS signal can be received, it might be unreliable for indoor situations. In that case, high stability frequency references, such as temperature-compensated crystal oscillators (TCXOs) with subpart per million (ppm) accuracy, can be used [44]. For example, a 1-ppm 10-MHz crystal would take 20 ms to have a 20% synchronization mismatch, which is extremely long compared to a symbol period of  $1.6 \mu\text{s}$  at 0.625 MSymbol/s.

The second challenge is code alignment. Any timing skew results in signal-to-noise ratio (SNR) reduction. However, the skew can be overcome by delaying the PN code with fixed digital delay steps and measuring the RX power for each step. Then, the correct delay is selected that maximizes the RX power. The code delay alignment can be updated regularly using digital logic gates with negligible power consumption.

Finally, synchronization is more challenging for moving objects compared to stationary radios due to the accompanied Doppler shift. Multiple techniques were previously proposed in CDMA systems to overcome this issue [45], [46]. Synchronization would also require changes in the FD physical layer frame requiring a synchronization preamble before data transmission and this preamble should be much shorter compared to the data frame to maintain FD BW efficiency.

In the demonstration, synchronization was achieved using a GPS disciplined oscillator (LeoBodnar) to provide a 10-MHz reference to the PN pattern generator (LinkInstruments). The pattern generator has 32 channel outputs that were sufficient for synchronizing 32 length PN codes. The synchronization test setup is shown in Fig. 6 where one USRP was transmitting QPSK signal spread by 32-length random PN code and the RX node was synchronized by observing the RX power. The measured synchronization profile is shown in Fig. 7 with a delay step of one chip period indicating a unique autocorrelation peak. Simulations indicate that the RX power

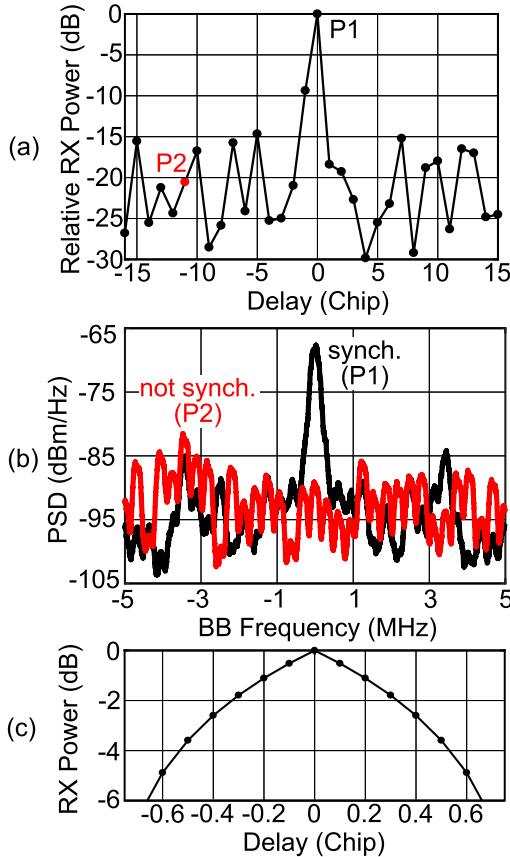


Fig. 7. Measured synchronization profile. (a) Relative RX power versus chip delay. (b) Illustrative RX spectrum for synchronized and non-synchronized cases. (c) Simulated synchronization profile near the peak.

is not affected by slight synchronization mismatch and the RX IL increases by only 1.1 dB for  $\pm 20\%$  synchronization offset, as shown in Fig. 7(c).

#### B. Out-of-Band Spectral Emissions

Another challenge in CD signal processing at RF is the spectral emission associated with the PN code spreading. RF transceivers should comply with a specific spectral mask as determined by the communication standard. Otherwise, out-of-band (OOB) emissions could harm other RXs operating in nearby bands. One obvious approach to reduce the OOB spectral leakage uses a SAW filter after the TX. However, measurements with a commercial SAW filter [47] indicate insufficient adjacent channel leakage suppression, as shown in Fig. 8(a).

Another approach to reduce the OOB spectral leakage is by applying the pulse-encoded transition (PET) technique described in [48]. The nearby OOB leakage can be greatly reduced through proper choice of the pulsedwidth of the used PN code, as shown in Fig. 8(c). Table I compares the effect of using a SAW filter and PET on the TX IL and the achieved adjacent channel leakage ratio (ACLR). The used PET technique reduces ACLR by  $>40$  dB for an extra 1.2 dB of IL, which is less than the SAW IL of 2.9 dB, thus presenting less degradation to the TX efficiency compared to SAW filters.

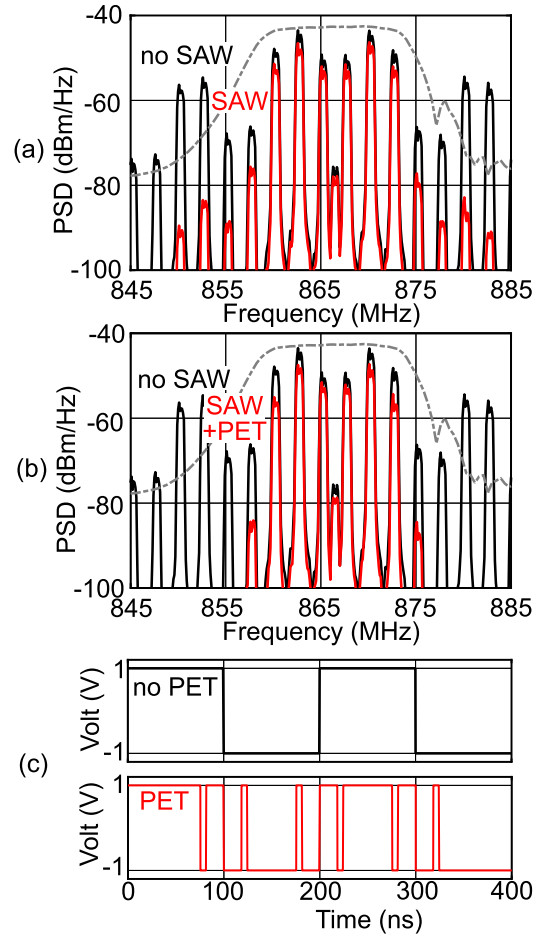


Fig. 8. Measured ACLR improvement with PET. (a) TX spectrum with limited ACLR rejection using a SAW filter. (b) TX spectrum with enhanced ACLR rejection with PET and SAW filter. (c) Added transitions on PN code for ACLR improvement.

TABLE I  
EFFECT OF PET ON IL AND ACLR

	TX IL (dB)	ACLR (dB)
No SAW	0	12.4
SAW	2.9	32.9
SAW + PET	4.1	40.1

#### C. Minimum Detectable Signal and PN Spurs

Modulating the RF front end with PN codes generates PN spurs in the RX spectrum. PN spurs are generated due to leakages and mismatches in the RF switches. PN spurs may pose a challenge in CD FD if not well taken care of when detecting signals near the sensitivity level of the RX.

Fig. 9(a) shows the measured error vector magnitude (EVM) for varying RX power level without PN codes and with different 16-length Walsh codes using the QPSK modulation. PN spurs degrade the RX EVM as the RX power approaches the noise floor of the RX. However, at a reasonable RX SNR, around 15 dB, the EVM differences become negligible.<sup>3</sup> Also, it was noticed that PN codes with spurs at higher frequency offset such as W2, which has the nearest spur at  $f_{\text{chip}}/2$  from

<sup>3</sup>PN spurs require an extra 3–4 dB in SNR for a targeted bit error rate (BER) of  $10^{-6}$  as QPSK requires an SNR of  $\sim 11$  dB.

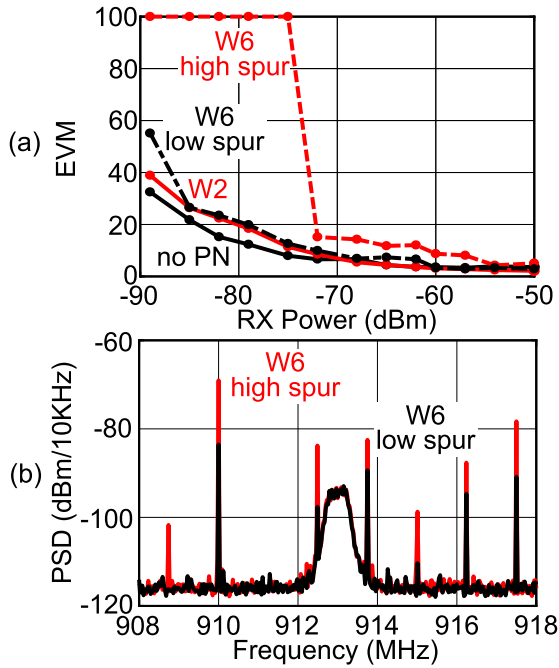


Fig. 9. Effect of PN spurs. (a) RX EVM versus RX power for different PN codes. (b) Measured RX spectrum with high and low W6 spurs.

the RX center frequency ( $f_{RF}$ ), have a better performance compared to other Walsh codes where the spurs lie closer to  $f_{RF}$ .

To confirm that the EVM degradation is due to PN spurs, two measurements were performed using the same Walsh code but at a different spur level. The spur level was controlled by varying the PN code signal swing, and the RX spectrum is shown for both cases in Fig. 9(b). It is evident from Fig. 9(a) that reducing the PN spur level greatly enhances the RX EVM. Also, a longer PN code reduces the spur level and the PN spur offset frequency is deterministic depending on the used PN code and the performance can still be enhanced using digital spur cancellation techniques as in [49].

#### IV. ADVANTAGES OF CODE-DOMAIN PROCESSING FOR FULL-DUPLEX COMMUNICATION

##### A. Linearity Improvement

FD links are designed to tolerate high TX power levels while receiving small desired RX signals. This places strict requirements on the rejection and linearity requirements of the TX–RX chain to handle the DR difference between the TX and RX signals. Nonlinear distortion generated in the TX–RX chain should be reduced to the RX sensitivity level for proper signal reception and becomes extremely important when using CMOS circulators, as analyzed in Section II-A.

In contrast to the nonlinearity of the PA that can be canceled through conventional RF cancellation techniques, the cancellation of distortion generated by the circulator is nontrivial as they are generated after the RF canceller tap. Based on (2), a circulator TX–RX IIP3 of 34 dBm is required to handle a 20-dBm TX signal.

Code-domain signal processing proves useful in relaxing the circulator IIP3 requirements in FD links. The IIP3 with

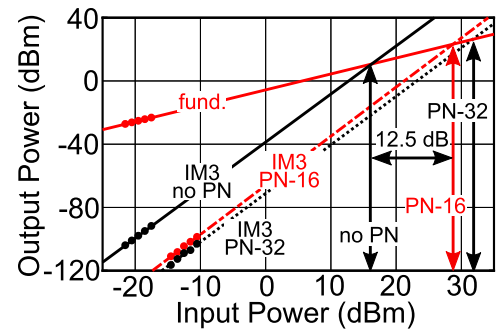


Fig. 10. IIP3 improvement for the RX modulator with PN codes.

PN code is enhanced by the PG of the used PN code,  $PG = 10 \log_{10}(M)$ , and is expressed as [28]

$$IIP3_{PN} = IIP3 + 10 \times \log_{10}(M) \quad (4)$$

where  $M$  is the code length. The circulator IIP3 is increased by 12 dB for 16-length PN code allowing >20-dBm TX power levels for the same RX sensitivity. Fig. 10 shows the effect of different PN codes on the RX modulator IIP3. The IIP3 increases from 16.25 dBm without PN codes to 28.75 dBm for 16-length PN code and further increases to 31.75 dBm for 32-length PN code confirming the theoretical prediction.

##### B. Blocker Tolerance

RF RXs operate in congested wireless channels demanding the RX to tolerate many blockers in addition to the TX SI. Radio regulation agencies, such as the Federal Communications Commission (FCC), regulate the spectrum by allocating different bands to different applications. Therefore, RF filters are used at the RF front end to remove blockers. These filters are usually implemented off-chip for better rejection raising the area and cost overhead. Moreover, RF radios could operate in hostile environments where jammers intend to obscure the RF communication link. RF CD signal processing relaxes the required filtering and blocker tolerance requirements due to the PG of the used PN code that spreads the unwanted blockers across the spread BW.

Fig. 11(a) shows the measured RX EVM versus the power of a continuous-wave (CW) IB blocker at 0.25-MHz offset. The desired RX signal is a QPSK signal at -60 dBm, while the IB blocker power is increased. Measurements indicate that without PN codes, the RX is desensitized even at a blocker power 10 dB less than the desired signal. Using 16-length PN codes enhances the blocker tolerance by 12.5 dB, whereas using 64-length codes enhances it by 17.5 dB for the same EVM level. These results are consistent with the PG of the used code.

The same experiment was repeated with an IB WB blocker (a QPSK signal with 10 MSymbol/s at the same center frequency). PN codes also proved to be tolerant of WB blockers, as shown in Fig. 11(b).

##### C. Multipath Tolerance

Another challenge in wireless environments is multipath propagation. As the TX signal propagates through different

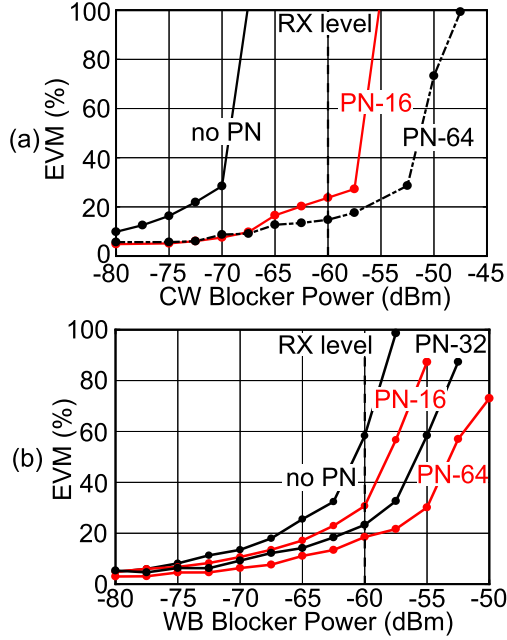


Fig. 11. Blocker tolerance of RF CD signal processing. (a) RX EVM versus IB CW blocker power without PN codes and with PN codes of different lengths. (b) RX EVM versus IB WB blocker power without PN codes and with PN codes of different lengths.

paths to the RX, the SNR can be harmed by fading and intersymbol interference (ISI) if the path delays are in the same order of magnitude as the symbol period.

Fig. 12 shows a typical wireless channel model based on the Stanford University Interim (SUI-4) channel model [50]. The wireless channel can be described as

$$h_C(t) = \sum_{i=1}^I h_{C,i} \delta(t - t_{C,i}) \quad (5)$$

where  $h_{C,i}$  and  $t_{C,i}$  are the gain and delay of the additive wireless channel paths, respectively. Consequently, the signal arriving at the RX antenna is

$$\text{RX}_{\text{in}}(t) = \text{TX}(t) * h_C(t) = \sum_{i=1}^I h_{C,i} \times \text{TX}(t - t_{C,i}) \quad (6)$$

indicating that the RX signal is deformed by the different multipath components.

RF CD signal processing proves to be resilient to multipath propagation. The PN-coded TX signal  $\text{TX}(t) = m(t) \times \text{PN}(t)$  reaches the RX after propagating through the multipath channel as

$$\text{RX}_{\text{in}}(t) = \sum_{i=1}^I h_{C,i} \times m(t - t_{C,i}) \times \text{PN}(t - t_{C,i}). \quad (7)$$

Upon arriving at the antenna, the RX signal is multiplied by a PN code corresponding to a specific tap delay (with the largest path gain). This allows rejecting other multipath components due to orthogonality between different delayed versions of the

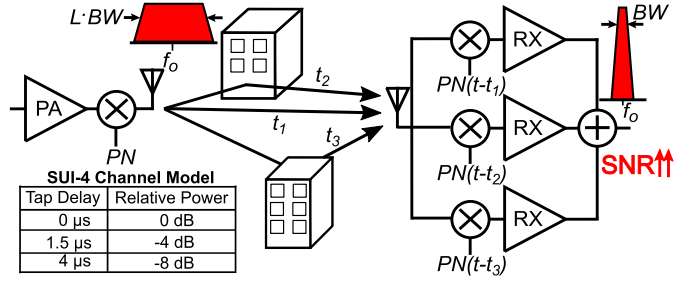


Fig. 12. Multipath channel based on the SUI-4 model.

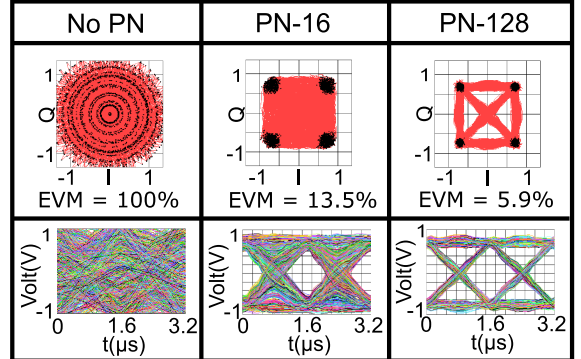


Fig. 13. Measured EVM and eye diagram for different PN code lengths in an SUI-4 multipath channel showing the advantage of PN codes in restoring RX eye diagram and EVM.

same PN code

$$\frac{1}{T} \int_T \text{PN}(t) \times \text{PN}(t - \tau) dt = 1/M \quad \forall \tau \neq 0 \quad (8)$$

$$\begin{aligned} \text{RX}_{\text{out}}(t) &= \text{PN}(t - t_{C,i}) \times \text{RX}_{\text{in}}(t) \\ &\approx h_{C,i} m_D(t - t_{C,i}). \end{aligned} \quad (9)$$

The RX modulator output is then passed down the RX chain to the LNA without being affected by multipath effects.

The proposed RX was tested in a multipath environment to show the effects of the used PN code on multipath resilience. A QPSK signal with 0.625 MSymbol/s was modulated by a PN code of varying length and filtered by the multipath channel (see Fig. 12) in MATLAB and generated by an arbitrary waveform generator (M8195a) to the proposed RX. The RX EVM and eye diagram were measured using Labview Software for 16/32/64/128 length PN code and without PN codes, as shown in Fig. 13. Measurements indicate that PN codes help in restoring the eye opening enabling correct reception despite multipath effects. Also, increasing the used PN code length results in a better RX EVM.

Another important advantage of using PN codes is that the RX can be configured to receive different multipath components by using different RX fingers each synchronized to a different tap known as "Rake RX" [51]. A simple rake RX implementation is shown in Fig. 12, and a low-power CMOS implementation was proposed in [52]. Fig. 14 shows the three-finger EVM and eye diagram for 128-length code, and Fig. 15 shows the measured spectrum for the three fingers. The measured RX power levels were -73.5, -78.4, and -81.5 dBm for the three fingers in agreement with the multipath channel model relative gains.

TABLE II  
MEASUREMENTS SUMMARY IN A MULTIPATH ENVIRONMENT

	no PN	PN-16	PN-32	PN-64	PN-128
1 <sup>st</sup> Finger EVM	NR	13.5%	12.8%	7.5%	5.9%
2 <sup>nd</sup> Finger EVM	NR	NR	NR	22.6%	9.2%
3 <sup>rd</sup> Finger EVM	NR	NR	14.5%	NR	26.8%

NR=Not Recognized

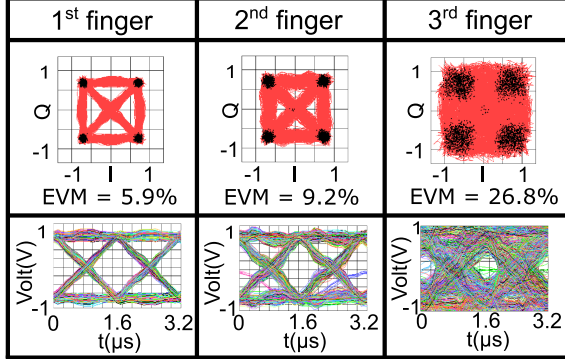


Fig. 14. Measured EVM and eye diagram for the three fingers of a rake RX with 128-length PN code in an SUI-4 multipath channel indicating correct reception of multipath components improving RX SNR.

Table II summarizes the results of the proposed RX with the multipath channel model and shows the advantages of increasing the PN code length on the RX signal SNR.

## V. CD FD TRANSCEIVER LINK MEASUREMENTS

The CD FD transceiver system was measured by generating a QPSK signal from the USRP TX port. The TX signal symbol rate was programmed between 0.625 and 3.125 MSymbol/s limited by the used hardware. Then, the TX signal was modulated by a 16-length Walsh PN code with a chip rate between 10 and 50 MChip/s depending on the used symbol rate. The Walsh code was generated by the Link Instruments pattern generator shown in Fig. 6. The modulated TX signal was amplified by a WB PA (ZHL-10W-2G+) for an integrated power between 10 and 30 dBm. The PA output signal passes through the CMOS circulator to the RX modulator with an orthogonal PN code, and the output of the RX modulator is connected to the USRP RX port for further signal processing.

An illustrative measured spectrum at various nodes of the transceiver is shown in Fig. 16 demonstrating the modulation of a 0.625-MSymbol/s 26-dBm TX signal by a Walsh code at 10 MChip/s and how the circulator rejection and RX code correlation increases the rejection of the TX signal.

For a complete characterization of the proposed CD FD transceiver, the rejection was measured at varying symbol rates, chip rates, and TX power levels. Also, different combinations of Walsh codes were experimented at different antenna terminations to investigate the interaction between spreading and circulator rejection BW on the achieved rejection.

### A. Performance With 50-Ω Termination

The rejection of the FD transceiver at the circulator RX port and after the RX modulator is shown in Fig. 17 when a broadband 50-Ω termination is used at the antenna port.

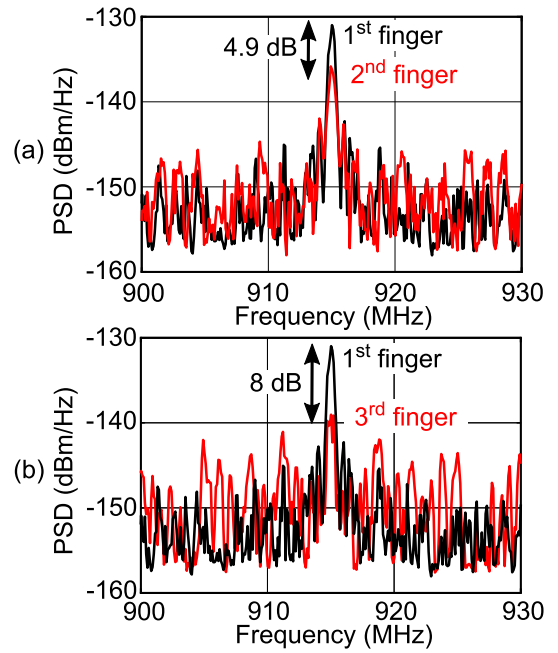


Fig. 15. Measured spectrum in an SUI-4 channel with 128-length PN code. (a) First finger versus second finger. (b) First finger versus third finger.

The circulator rejection across the spread BW reaches 46.9 dB at 20-dBm TX power and 10-MChip/s chip rate and the rejection decreases at higher chip rates and TX power levels, as shown in the left of Fig. 17.

The combined circulator and code rejection across the signal BW depends on the choice of PN codes [28]. For example, Walsh codes W1 and W2 offer better rejection relative to Walsh codes W5 and W6 due to the robustness of the orthogonality to BW limitations. Measurements demonstrate that a maximum rejection of 90.5 dB is possible with W1 and W2 Walsh code pairs (see Fig. 17 middle). When using W5 and W6 code pairs, the rejection reduces to 79 dB (see Fig. 17 right). It was also observed that the TX power peak rejection depends on the code spreading properties suggesting that the rejection can be optimized by retuning the circulator at different TX power levels for different PN codes.

### B. Performance With Antenna Termination

The same experiment was repeated with the circulator connected to a COTS VERT900 antenna. The measured circulator TX–RX isolation with the antenna after tuning the feed capacitors is shown in Fig. 4(b) compared to that with a 50-Ω termination. The rejection BW of the circulator is reduced due to the antenna, and the achieved circulator rejection depends on the effective signal BW over which the TX signal is spread. Fig. 18 shows that the combined circulator and code rejection drops to 56 dB for W5 and W6 and to 70.9 dB for W1 and W2 code pairs representing around 20-dB degradation compared with 50-Ω termination.

This degradation can be attributed to the GD variation between the TX and RX ports of the circulator when connected to the antenna. Fig. 19 shows the measured GD between the TX and RX ports with 50 Ω and antenna termination. The TX–RX peak GD increases from 13 to 84 ns when

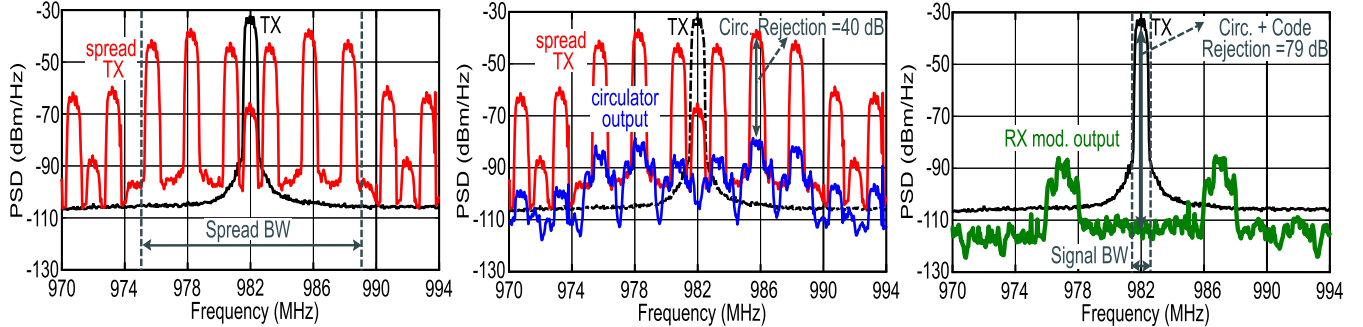


Fig. 16. Measured spectrum at various nodes of the transceiver. Left: TX modulated spectrum at 26 dBm. Middle: circulator RX output with 40-dB rejection. Right: RX modulator output showing combined circulator and code rejection of 79 dB.

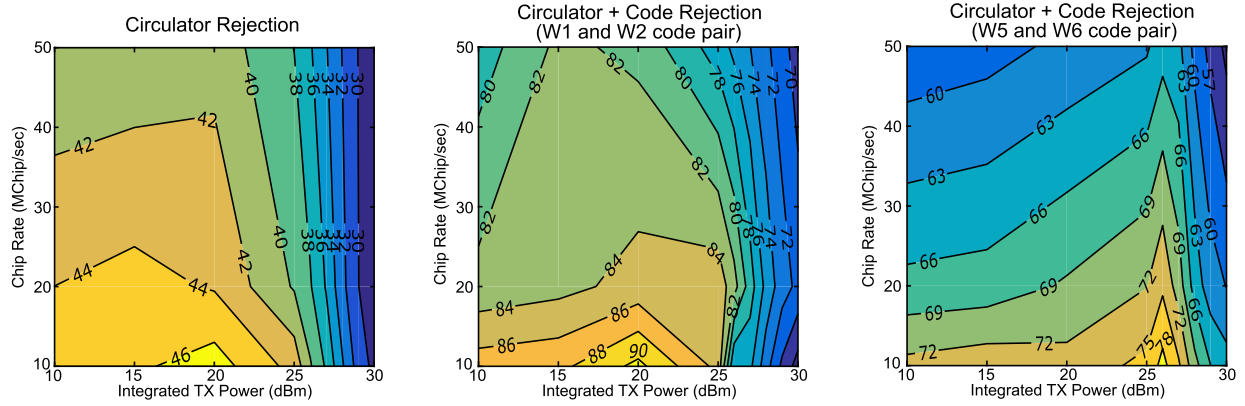


Fig. 17. Measured rejection of the FD system in a  $50\Omega$  environment at different power levels and chip rates. Left: circulator rejection. Middle: circulator and code rejection using optimum 16-length Walsh code pairs (W1 and W2). Right: circulator and code rejection using other Walsh code pairs (W5 and W6).

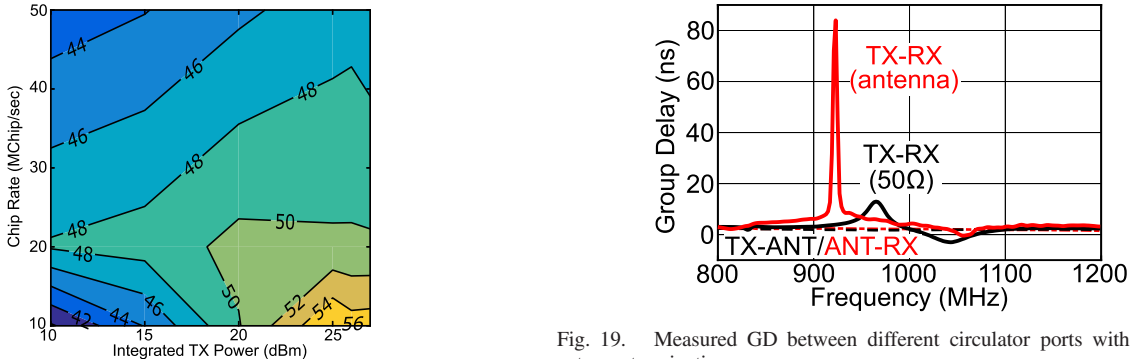


Fig. 18. Measured circulator and code rejection with an antenna (W5 and W6).

adding the VERT900 antenna. This GD variation across the spread BW degrades the Walsh codes orthogonality as the GD approaches the used chip period (100 ns at 10 MChip/s). The GD between the TX-ANT and ANT-RX ports was negligible compared to that between the TX-RX ports presenting no limitation on signal transmission or reception. The rejection can be improved using a broadband antenna with less VSWR variations across the spread BW, given that high circulator rejection is maintained until 2.33 VSWR through the feed-capacitors' tuning network.

#### C. Overall Rejection With Digital SIC

Finally, digital SIC was applied to the IQ BB data from the USRP, as detailed in Section II-C. Fig. 20(a) shows the results of applying digital SIC for the best case rejection where digital

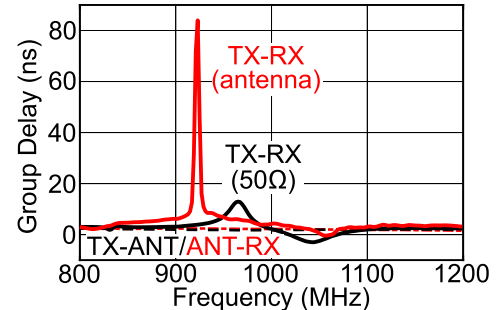


Fig. 19. Measured GD between different circulator ports with  $50\Omega$  and antenna termination.

SIC was adding 13.6-dB rejection to the 90.5 dB achieved in the RF domain for a total of 104.1 dB. The overall rejection brings the 20-dBm TX power to the noise floor of the USRP around  $-85$  dBm.<sup>4</sup>

Using the VERT900 antenna, digital SIC adds 26 dB to the 70.9 dB of RF rejection for a total of 96.9 dB at 15 dBm and 27 dB to the 68.2 dB of RF rejection for a total of 95.2 dB at 23.5 dBm, as shown in Fig. 20(b). Digital SIC was more effective with antenna termination due to higher SI level confirming Fig. 5(a) and was limited by the noise floor in both cases of  $50\Omega$  and antenna termination. An NF degradation of 2–3 dB was observed in the USRP noise floor after connecting the antenna due to the measurement

<sup>4</sup>The noise floor is degraded by  $\sim 3$  dB from the theoretically calculated value of  $-88$  dBm due to TX induced NF from the circulator switches as the reported 2.5-dB NF of the circulator was measured without a TX signal and applying a TX signal increases the circulator NF.

TABLE III  
PERFORMANCE SUMMARY AND COMPARISON

	Antenna Interface	Freq. (GHz)	Antenna Rej. (dB)	RF Rej. (dB)	Digital Rej. (dB)	Total Rej. (dB)	TX Power (dBm)	BW (MHz)	FOM (dBm.MHz)
Asilomar'10 [6]	2 Ant.	2.4	45	31	4	80	15	0.625	93
MobiCom'11 [7]	2 Ant.	2.45		45	28	73	12 <sup>1</sup>	10	95
CoRR'11 [8]	2 Ant.	2.4	57	24	NA	81	6	10	97
Sigcomm'13 [13]	Magn. Circ.	2.45		72/62	38/48	110	25/20	20/80	148/149
GLOBECOM'15 [14]	Magn. Circ.	2.46		79/56	31.9/45.9	110.9/101.9	16.5/13.3	1.4/20	128.9/128.2
IMS'15 [9]	Ant. Array	2.45	81.8 <sup>1</sup>	14.2	NA	96	22.7	30	133.5
VTC'15 [19]	EBD	0.89/1.89	44/45	41/38	NA	85/83	10	20	108/106
Comm. Mag.'16 [15]	Magn. Circ.	2.45	19.9/22.2	48.3/40.9	25.3/24.7	93.5/87.8	6.4/8	20/80	112.9/114.8
Wireless Comm.'16 [10]	Isol. Ant.	2.45	56/56.4	21.9/13.3	NA	77.9/69.7	30	20/120	120.9/120.5
GLOBECOM'17 [17]	Magn. Circ. <sup>2</sup>	0.9	21	36	34	91	20	20	124
INFOCOM'17 [16]	Magn. Circ.	0.9		50	45	95	5	5	107
Ant. & Prop. '17 [11]	Anechoic Indoors	2.56	75.5	16.9/7	22.9/24.6	115.3/107.2	29/28.5	20/80	157.3/154.7
Wireless Comm.'18 [12]	Pol. Ant.	3.5	41.9	NA	43/39.9	107.1/103.4	24.2/23.7	40/80	147.3/146.1
ICC'19 [20]	CMOS Circ.	1		55	40	95	15	3.5 <sup>3</sup>	115.4
This Work	50 Ohm Antenna	1	45.5	45 <sup>4</sup>	13.6	104.1	20	1.25 <sup>5</sup>	125.1
	CMOS circ.		35.9/37.4	35/30.8 <sup>4</sup>	26/27	96.9/95.2	15/23.5		112.9/119.7

<sup>1</sup>with spatial beamforming, <sup>2</sup>with passive antenna emulation, <sup>3</sup>estimated from plot, <sup>4</sup>RF code domain rejection, <sup>5</sup>signal BW spread at 10Mchip/sec

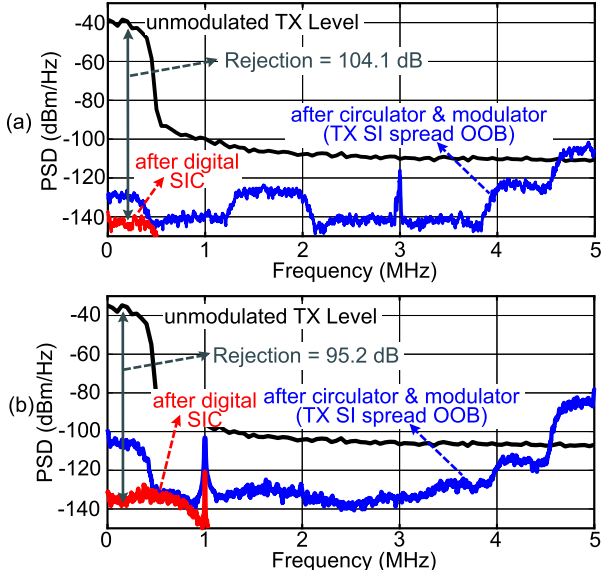


Fig. 20. Measured overall rejection with digital SIC. (a) 104.1 dB of rejection at 20-dBm TX power with 50- $\Omega$  termination. (b) 95.2 dB of rejection at 23.5-dBm TX power with antenna termination.

environment and this slightly reduced the achieved rejection compared to the peak digital rejection in Fig. 5(a). The total rejection and symbol rate can be improved by combining other RF/analog cancellation techniques with a better broadband antenna along with a lower noise RX with higher ADC sampling rates increasing the FD transceiver overall rejection.

#### D. Performance Summary and FD Figure of Merit

Table III summarizes the performance of the proposed CD FD transceiver and how it compares with state-of-the-art literature. Fig. 21 compares the achieved figure of merit (FOM) of the proposed transceiver with that of other FD transceivers in the literature. Table III and Fig. 21 focused on comparing the proposed work with full system FD implementations that span multiple SI rejection techniques for a fair comparison. The FOM is similar to that defined in [3] and is given by

$$\text{FOM} = \text{REJ} \times P_{\text{TX}} \times \text{BW} \quad (10)$$

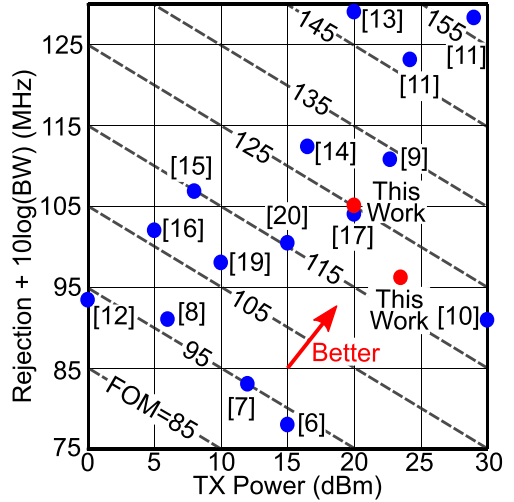


Fig. 21. FOM comparison for different architectures in Table III.

where REJ is the total system TX SI rejection in linear units, BW is the bandwidth in MHz, and  $P_{\text{TX}}$  is the TX output power in milliwatts. While there are other important factors to consider in FD systems (such as power consumption and NF), these were not included in the FOM as most FD systems spanning multiple rejection domains relied on SDRs, field-programmable gate arrays (FPGAs), or standard measurement equipment as their implementation platform and these factors were rarely mentioned in the respective papers. The FOM only considers three metrics of the FD transceiver (REJ,  $P_{\text{TX}}$ , and BW) as they are the most important factors for FD systems and were reported in all FD systems papers.

Rejection is clearly an important factor and the TX power level that can be handled is an extremely challenging problem given the linearity requirements of the RX. Also, the BW over which the rejection is achieved is an important factor to consider as achieving high rejection over a wide BW is a challenging problem for FD systems given the large variations in the frequency response of the SI channel.

The proposed CD FD transceiver achieves an FOM of 125.1 and 119.7 dBm-MHz with 50  $\Omega$  and COTS antenna

termination. The FOM was calculated using the signal BW of 1.25 MHz for a fair comparison with other work that does not apply signal spreading. However, the FOM would increase to 137.1 dBm·MHz if the spread BW was used and it can be justified by noting that the overall system BW efficiency is not affected by spreading as we can have multiple transceivers operating in the same spread BW such that each transceiver uses an orthogonal PN code, given that the system uses PN codes with good cross-correlation properties to maintain rejection and system capacity along with network coordination to assign and synchronize codes for the simultaneous users.

The Appendix briefly discusses various PN code families for CD systems indicating the availability of various codes with good cross correlation. It is also evident that increasing the used code length is advantageous for the proposed FD system (improved PG, multipath tolerance, and so on), but this requires a tradeoff between the used symbol rate and spread BW. Increasing the code length for a fixed symbol rate requires higher spread BW dictating higher circulator BW and ADC sampling rate, whereas increasing the code length for a fixed spread BW would severely limit the used symbol rate. Other tradeoffs for longer codes also exist, such as synchronization and increased system latency. However, this can be alleviated by using better synchronization algorithms. CD FD systems with 32 length codes at 64-MChip/s chip rate and 2-MSymbol/s symbol rate seem feasible, and continued research in FD systems would certainly result in better systems.<sup>5</sup>

## VI. CONCLUSION

This article presents a CD FD transceiver with around 100-dB TX SI rejection at >20-dBm TX power levels. The CD transceiver operates by spreading/despreading the TX/RX signals in the RF domain to achieve rejection due to the orthogonality of different TX/RX PN codes. The FD transceiver also uses a multiwatt, high-rejection CMOS circulator and digital SIC to improve the achieved rejection. Measurements indicate a CD FD technique that is tolerant to TX SI as well as IB CW and modulated blockers. Moreover, orthogonality between the delayed PN codes proves useful in practical wireless environments providing tolerance to multipath propagation effects and reflections.

## APPENDIX

### CODE SELECTION FOR CODE-DOMAIN SYSTEMS

Multiple PN code families were used in CDMA and WB CDMA (WCDMA) systems that can be employed in the proposed CD FD transceiver to extend its operation to multiple user systems while maintaining system capacity and rejection. This section presents a brief overview of different code families and an extensive discussion can be found in [53] and [54].

Walsh codes of length  $M$  are constructed with

$$W_2 = \begin{bmatrix} 1 & 1 \\ 1 & -1 \end{bmatrix}; \quad W_{2^k} = \begin{bmatrix} W_{2^{k-1}} & W_{2^{k-1}} \\ W_{2^{k-1}} & -W_{2^{k-1}} \end{bmatrix} \quad (11)$$

<sup>5</sup>CDMA started with 14.4 Kb/s in IS-95 and eventually reached 10 Mb/s in WCDMA [53].

where  $k = \log_2(M)$ . Walsh codes were used in the proposed system for their good rejection properties and ease of generation with the used pattern generator, but they suffer from bad synchronization due to repetitive nature and limited number of available codes.

$M$ -sequences are odd-length sequences with code length  $M = 2^n - 1$ , where  $n$  is an integer. The autocorrelation is either 1 or  $-1/M$ , which guides synchronization. The cross correlation, however, takes large values, which degrades rejection. Nevertheless, Gold codes can be generated by XORing a subset of preferred  $m$ -sequences to bound the cross correlation improving code rejection.

A practical system uses a combination of different codes for multiuser operation to guarantee rejection and system capacity. For example, long codes based on scrambling different sequences were used in WCDMA systems to further extend the code space as described in [53].

## ACKNOWLEDGMENT

The authors would like to thank Dr. T. Hancock and Dr. T. Olsson through the DARPA Signal Processing at RF (SPAR) Program for useful discussion.

## REFERENCES

- [1] A. Sabharwal, P. Schniter, D. Guo, D. W. Bliss, S. Rangarajan, and R. Wichman, "In-band full-duplex wireless: Challenges and opportunities," *IEEE J. Sel. Areas Commun.*, vol. 32, no. 9, pp. 1637–1652, Sep. 2014.
- [2] G. Liu, F. R. Yu, H. Ji, V. C. M. Leung, and X. Li, "In-band full-duplex relaying: A survey, research issues and challenges," *IEEE Commun. Surveys Tuts.*, vol. 17, no. 2, pp. 500–524, 2nd Quart., 2015.
- [3] K. E. Kolodziej, B. T. Perry, and J. S. Herd, "In-band full-duplex technology: Techniques and systems survey," *IEEE Trans. Microw. Theory Techn.*, vol. 67, no. 7, pp. 3025–3041, Jul. 2019.
- [4] J. I. Choi, M. Jain, K. Srinivasan, P. Levis, and S. Katti, "Achieving single channel, full duplex wireless communication," in *Proc. 16th Annu. Int. Conf. Mobile Comput. Netw.*, 2010, pp. 1–12.
- [5] E. Everett, A. Sahai, and A. Sabharwal, "Passive self-interference suppression for full-duplex infrastructure nodes," *IEEE Trans. Wireless Commun.*, vol. 13, no. 2, pp. 680–694, Feb. 2014.
- [6] M. Duarte and A. Sabharwal, "Full-duplex wireless communications using off-the-shelf radios: Feasibility and first results," in *Proc. Conf. Rec. Forty 4th Asilomar Conf. Signals, Syst. Comput.*, Nov. 2010, pp. 1558–1562.
- [7] M. Jain *et al.*, "Practical, real-time, full duplex wireless," in *Proc. 17th Annu. Int. Conf. Mobile Comput. Netw.*, 2011, pp. 301–312.
- [8] A. Sahai, G. Patel, and A. Sabharwal, "Pushing the limits of full-duplex: Design and real-time implementation," *CoRR*, vol. abs/1107.0607, pp. 1–12, Jul. 2011.
- [9] K. E. Kolodziej, B. T. Perry, and J. S. Herd, "Simultaneous transmit and receive (STAR) system architecture using multiple analog cancellation layers," in *IEEE MTT-S Int. Microw. Symp. Dig.*, May 2015, pp. 1–4.
- [10] K. E. Kolodziej, J. G. McMichael, and B. T. Perry, "Multitap RF canceller for in-band full-duplex wireless communications," *IEEE Trans. Wireless Commun.*, vol. 15, no. 6, pp. 4321–4334, Jun. 2016.
- [11] D. Korpi, M. Heino, C. Icheln, K. Haneda, and M. Valkama, "Compact inband full-duplex relays with beyond 100 dB self-interference suppression: Enabling techniques and field measurements," *IEEE Trans. Antennas Propag.*, vol. 65, no. 2, pp. 960–965, Feb. 2017.
- [12] H. Li *et al.*, "Self-interference cancellation enabling high-throughput short-reach wireless full-duplex communication," *IEEE Trans. Wireless Commun.*, vol. 17, no. 10, pp. 6475–6486, Oct. 2018.
- [13] D. Bharadwaj, E. McMillin, and S. Katti, "Full duplex radios," *ACM SIGCOMM Comput. Commun. Rev.*, vol. 43, no. 4, pp. 375–386, Sep. 2013.
- [14] D. Korpi, Y.-S. Choi, T. Huusari, L. Anttila, S. Talwar, and M. Valkama, "Adaptive nonlinear digital self-interference cancellation for mobile inband full-duplex radio: Algorithms and RF measurements," in *Proc. IEEE Global Commun. Conf.*, Dec. 2015, pp. 1–7.

- [15] D. Korpi *et al.*, "Full-duplex mobile device: Pushing the limits," *IEEE Commun. Mag.*, vol. 54, no. 9, pp. 80–87, Sep. 2016.
- [16] T. Chen, J. Zhou, M. B. Dastjerdi, J. Diakonikolas, H. Krishnaswamy, and G. Zussman, "Demo abstract: Full-duplex with a compact frequency domain equalization-based RF canceller," in *Proc. IEEE Conf. Comput. Commun. Workshops*, May 2017, pp. 972–973.
- [17] M. Emara, P. Rosson, K. Roth, and D. Dassonneville, "A full duplex transceiver with reduced hardware complexity," in *Proc. IEEE Global Commun. Conf.*, Dec. 2017, pp. 1–6.
- [18] L. Laughlin, M. A. Beach, K. A. Morris, and J. L. Haine, "Electrical balance duplexing for small form factor realization of in-band full duplex," *IEEE Commun. Mag.*, vol. 53, no. 5, pp. 102–110, May 2015.
- [19] L. Laughlin, C. Zhang, M. A. Beach, K. A. Morris, and J. Haine, "A widely tunable full duplex transceiver combining electrical balance isolation and active analog cancellation," in *Proc. IEEE 81st Veh. Technol. Conf. (VTC Spring)*, May 2015, pp. 1–5.
- [20] A. Nagulu, T. Chen, G. Zussman, and H. Krishnaswamy, "A single antenna full-duplex radio using a non-magnetic, CMOS circulator with in-built isolation tuning," in *Proc. IEEE Int. Conf. Commun. Workshops (ICC Workshops)*, May 2019, pp. 1–6.
- [21] N. Reiskarimian, A. Nagulu, T. Dinc, and H. Krishnaswamy, "Nonreciprocal electronic devices: A hypothesis turned into reality," *IEEE Microw. Mag.*, vol. 20, no. 4, pp. 94–111, Apr. 2019.
- [22] A. Nagulu, N. Reiskarimian, and H. Krishnaswamy, "Non-reciprocal electronics based on temporal modulation," *Nature Electron.*, vol. 3, no. 5, pp. 241–250, May 2020.
- [23] A. Nagulu, A. Gaonkar, S. Ahasan, T. Chen, G. Zussman, and H. Krishnaswamy, "A full-duplex receiver leveraging multiphase Switched-Capacitor-Delay based multi-domain FIR filter cancelers," in *Proc. IEEE Radio Freq. Integr. Circuits Symp. (RFIC)*, Aug. 2020, pp. 43–46.
- [24] J. Zhou, T.-H. Chuang, T. Dinc, and H. Krishnaswamy, "19.1 receiver with >20MHz bandwidth self-interference cancellation suitable for FDD, co-existence and full-duplex applications," in *IEEE Int. Solid-State Circuits Conf. (ISSCC) Dig. Tech. Papers*, Feb. 2015, pp. 1–3.
- [25] D. Yang, H. Yuksel, and A. Molnar, "A wideband highly integrated and widely tunable transceiver for in-band full-duplex communication," *IEEE J. Solid-State Circuits*, vol. 50, no. 5, pp. 1189–1202, May 2015.
- [26] J. Zhou, N. Reiskarimian, and H. Krishnaswamy, "9.8 receiver with integrated magnetic-free N-path-filter-based non-reciprocal circulator and baseband self-interference cancellation for full-duplex wireless," in *IEEE Int. Solid-State Circuits Conf. (ISSCC) Dig. Tech. Papers*, Jan. 2016, pp. 178–179.
- [27] N. Reiskarimian, M. B. Dastjerdi, J. Zhou, and H. Krishnaswamy, "Analysis and design of commutation-based circulator-receivers for integrated full-duplex wireless," *IEEE J. Solid-State Circuits*, vol. 53, no. 8, pp. 2190–2201, Aug. 2018.
- [28] A. Hamza, C. Hill, H. AlShammary, and J. Buckwalter, "High-rejection RF code domain receivers for simultaneous transmit and receive applications," *IEEE J. Solid-State Circuits*, vol. 55, no. 7, pp. 1909–1921, Jul. 2020.
- [29] A. Hamza *et al.*, "A full-duplex transceiver with CMOS RF circulation and code-domain signal processing for 104 dB self-interference rejection and watt level TX power handling," in *IEEE MTT-S Int. Microw. Symp. Dig.*, Aug. 2020, pp. 1207–1210.
- [30] *Universal Software Radio Peripheral*, Nat. Instrum., Austin, TX, USA, Dec. 2016.
- [31] *Ettus Research*. Accessed: May, 1, 2020. [Online]. Available: <https://www.ettus.com/product/details/VERT900>
- [32] (May 2019). *CF1020 SMA/Female Circulator 1.0-2.0 GHz*. [Online]. Available: <https://www.centricrf.com/content/pdf/CF1020.pdf>
- [33] A. Nagulu, A. Alu, and H. Krishnaswamy, "Fully-integrated non-magnetic 180nm SOI circulator with >1W P1dB, >+50dBm IIP3 and high isolation across 1.85 VSWR," in *Proc. IEEE Radio Freq. Integr. Circuits Symp. (RFIC)*, Jun. 2018, pp. 104–107.
- [34] A. Nagulu, T. Chen, G. Zussman, and H. Krishnaswamy, "29.3 non-magnetic 0.18  $\mu$ m SOI circulator with multi-watt power handling based on switched-capacitor clock boosting," in *IEEE Int. Solid-State Circuits Conf. (ISSCC) Dig. Tech. Papers*, Feb. 2020, pp. 444–446.
- [35] *ZMQ-1050: Coaxial QPSK Modulator datasheet*, *Mini-Circuits*. Accessed: May 1, 2020. [Online]. Available: <https://www.minicircuits.com/pdfs/ZMQ-1050.pdf>
- [36] A. Ershadi and K. Entesari, "A 0.5-to-3.5-GHz full-duplex mixer-first receiver with Cartesian synthesized self-interference suppression interface in 65-nm CMOS," *IEEE Trans. Microw. Theory Techn.*, vol. 68, no. 6, pp. 1995–2010, Jun. 2020.
- [37] H. AlShammary, C. W. Hill, A. Hamza, and J. F. Buckwalter, "A code-domain RF signal processing front-end for simultaneous transmit and receive with 49.5 dB self-interference rejection, 12.1 dBm receive compression, and 34.3 dBm transmit compression," in *Proc. IEEE Radio Freq. Integr. Circuits Symp. (RFIC)*, Jun. 2019, pp. 143–146.
- [38] A. Hamza, H. AlShammary, C. Hill, and J. Buckwalter, "A 52-dB self-interference rejection receiver using RF code-domain signal processing," in *Proc. IEEE Custom Integr. Circuits Conf. (CICC)*, Apr. 2019, pp. 1–4.
- [39] C. Hill, C. S. Levy, H. AlShammary, A. Hamza, and J. F. Buckwalter, "RF watt-level Low-Insertion-Loss high-bandwidth SOI CMOS switches," *IEEE Trans. Microw. Theory Techn.*, vol. 66, no. 12, pp. 5724–5736, Dec. 2018.
- [40] C. Hill, A. Hamza, H. AlShammary, and J. F. Buckwalter, "A 1.5-dB insertion loss, 34-dBm P1dB power modulator with 46% fractional bandwidth in 45-nm CMOS SOI," in *IEEE MTT-S Int. Microw. Symp. Dig.*, Jun. 2019, pp. 243–246.
- [41] *ZHL-10W-2G+: Coaxial High Power Amplifier, Mini-Circuits*. Accessed: May 1, 2020. [Online]. Available: <https://www.minicircuits.com/pdfs/ZHL-10W-2G.pdf>
- [42] *PXIe-5645: Reconfigurable 6 GHz Vector Signal Transceiver with I/Q Interface*. Accessed: May 15, 2020. [Online]. Available: <https://www.ni.com/pdf/manuals/373914f.pdf>
- [43] M. A. Lombardi, "The use of GPS disciplined oscillators as primary frequency standards for calibration and metrology laboratories," *NCSLI Measure*, vol. 3, no. 3, pp. 56–65, Sep. 2008.
- [44] SiTime. *60 to 220 MHz, ±0.5 to ±2.5 ppm Super-TCXO*. Accessed: May 15, 2020. [Online]. Available: <https://www.sitime.com/datasheet/SiT5157>
- [45] K. Nakamura, K. Tajima, and M. Hieda, "A frequency synchronization scheme for time varying Doppler-shift compensation using the direct return signal," in *IEEE MTT-S Int. Microw. Symp. Dig.*, May 2016, pp. 1–3.
- [46] A. Kajiwara, "Mobile satellite CDMA system robust to Doppler shift," in *Proc. IEEE Int. Conf. Commun.*, May 1993, pp. 448–452.
- [47] *SF2314E: Low-loss 866.5 MHz SAW Filter datasheet*. Accessed: May 1, 2020. [Online]. Available: <https://wireless.murata.com/pub/RFM/data/sf2314e.pdf>
- [48] C. Hill, A. Hamza, H. AlShammary, and J. F. Buckwalter, "Watt-level, direct RF modulation in CMOS SOI with pulse-encoded transitions for adjacent channel leakage reduction," *IEEE Trans. Microw. Theory Techn.*, vol. 67, no. 12, pp. 5315–5328, Dec. 2019.
- [49] Y. Tang *et al.*, "A configurable multi-band multi-mode transmitter with spur cancellation through digital baseband," in *Proc. IEEE Symp. VLSI Circuits (VLSI)*, Jun. 2011, pp. 28–29.
- [50] V. Erceg. (Jul. 2001). *Channel Models for Fixed Wireless Applications*. [Online]. Available: [www.ieee802.org/16/tg3/contrib/802163c-01\\_29r4.pdf](http://www.ieee802.org/16/tg3/contrib/802163c-01_29r4.pdf)
- [51] R. Price and P. Green, "A communication technique for multipath channels," *Proc. IRE*, vol. 46, no. 3, pp. 555–570, Mar. 1958.
- [52] A. Hamza, C. Hill, H. AlShammary, and J. Buckwalter, "A Self-Interference-tolerant, multipath rake receiver with more than 40-dB rejection and 9-dB SNR multipath gain in a fading channel," in *Proc. IEEE Radio Freq. Integr. Circuits Symp. (RFIC)*, Aug. 2020, pp. 51–54.
- [53] H. Holma and A. Toskala, *WCDMA for UMTS*. Hoboken, NJ, USA: Wiley, 2001.
- [54] J. Proakis and M. Salehi, *Digital Communications*. New York, NY, USA: McGraw-Hill, 2008.



**Ahmed Hamza** (Graduate Student Member, IEEE) received the B.Sc. and M.Sc. degrees in electronics and communications systems engineering from Ain Shams University, Cairo, Egypt, in 2012 and 2016, respectively. He is currently pursuing the Ph.D. degree at the University of California at Santa Barbara, Santa Barbara, CA, USA.

His research interests include RF and millimeter-wave integrated circuits, and analog/mixed-signal design for wireline and wireless applications.

Mr. Hamza was a recipient of the Best Student Paper Award of the 2015 IEEE International Conference on Electronics, Circuits, and Systems and the UCSB ECE Department Ph.D. Dissertation Fellowship in 2020. He serves as a Reviewer for the IEEE JOURNAL OF SOLID-STATE CIRCUITS and the IEEE TRANSACTIONS ON MICROWAVE THEORY AND TECHNIQUES.



**Aravind Nagulu** (Member, IEEE) received the B.Tech. and M.Tech. degrees in electrical engineering from IIT Madras, Chennai, India, in 2016. He is currently pursuing the Ph.D. degree in electrical engineering at Columbia University, New York, NY, USA.

During his master's studies, he was involved in the implementation of a high-resolution continuous-time delta-sigma modulator. His current research focuses on exploring new directions to achieve fully integrated, magnetless nonreciprocity, and to provide experimental validation for nonreciprocal components catering a wide range of applications ranging from RF/millimeter-wave communication, frequency-modulated continuous wave (FMCW) radars, and quantum information processing.

Mr. Nagulu was a recipient of the IEEE RFIC Symposium Best Student Paper Award (First Place) in 2018, the IEEE Solid-State Circuits Society Predoctoral Achievement Award, the ISSCC Analog Devices Outstanding Student Designer Award, and the IEEE MTT-S Graduate Fellowship in 2019.



**Hussam AlShammary** (Member, IEEE) received the B.S. degree (Hons.) in electrical engineering from the King Fahd University of Petroleum and Minerals (KFUPM), Dhahran, Saudi Arabia, the M.S. degree from Carnegie Mellon University, Pittsburgh, PA, USA, in 2014, and the Ph.D. degree in electrical and computer engineering from the University of California at Santa Barbara, Santa Barbara, CA, USA, in 2019.

In 2019, he had an internship with Skyworks Solutions, San Jose, CA, USA, where he designed radio frequency integrated circuits for 5G NR applications. His research interests include RF/mixed-signal integrated circuit design and CMOS signal-processing techniques.



**Alfred Festus Davidson** (Graduate Student Member, IEEE) received the B.Tech. (Hons.) and M.Tech. degrees in electrical engineering from IIT Madras, Chennai, India, in 2020. He is currently pursuing the Ph.D. degree in electrical engineering at Columbia University, New York, NY, USA.

He was a Visiting Student with Columbia University in the summer of 2019. His current research interests include the design of integrated circuits and systems for next-generation communication paradigms, and the mathematical formulation and co-optimization of the RF/millimeter-wave, analog, and digital sections of the hardware implementations of these paradigms.

Mr. Davidson was selected for the S. N. Bose Scholars Program in 2019 and was a recipient of the Columbia University Presidential Fellowship in 2020.



**Harish Krishnaswamy** (Member, IEEE) received the B.Tech. degree in electrical engineering from IIT Madras, Chennai, India, in 2001, and the M.S. and Ph.D. degrees in electrical engineering from the University of Southern California (USC), Los Angeles, CA, USA, in 2003 and 2009, respectively.

In 2009, he joined the Electrical Engineering Department, Columbia University, New York, NY, USA, where he is currently an Associate Professor and the Director of the Columbia High-Speed and Millimeter-Wave IC Laboratory (CoSMIC). In 2017, he co-founded MixComm Inc., Chatham, NJ, USA, a venture-backed startup, to commercialize CoSMIC Laboratory's advanced wireless research. His current research interests include integrated devices, circuits, and systems for a variety of RF, millimeter-wave (mmWave), and sub-mmWave applications.

Dr. Krishnaswamy has been a member of the Technical Program Committee of several conferences, including the IEEE International Solid-State Circuits Conference since 2015 and the IEEE Radio Frequency Integrated Circuits Symposium since 2013. He was a recipient of the IEEE International Solid-State Circuits Conference Lewis Winner Award for Outstanding Paper in 2007, the Best Thesis in Experimental Research Award from the USC Viterbi School of Engineering in 2009, the Defense Advanced Research Projects Agency Young Faculty Award in 2011, the 2014 IBM Faculty Award, the Best Demo Award at the 2017 IEEE ISSCC, best student paper awards (First Place) at the 2015 and 2018 IEEE Radio Frequency Integrated Circuits Symposium, and the 2019 IEEE MTT-S Outstanding Young Engineer Award. He also serves as a Distinguished Lecturer for the IEEE Solid-State Circuits Society and a member for the DARPA Microelectronics Exploratory Council.



**Jonathan Tao** (Student Member, IEEE) received the B.S. degrees in electrical engineering and computer engineering from the University of California at Davis, Davis, CA, USA, in 2016. He is currently pursuing the Ph.D. degree in electrical and computer engineering at the University of California at Santa Barbara, Santa Barbara, CA, USA.

From 2017 to 2019, he was an Engineer with Tesla, Inc., Palo Alto, CA, USA. His research interests include signal processing and millimeter-wave circuit design.



**Cameron Hill** (Member, IEEE) received the B.E. and M.E. degrees in electrical and computer engineering from the Stevens Institute of Technology, Hoboken, NJ, USA, in 2015, and the Ph.D. degree in electrical and computer engineering from the University of California at Santa Barbara, Santa Barbara, CA, USA, in 2020.

He is currently continuing his work as a Post-Doctoral Researcher with the RF and Mixed-signal Integrated Circuits Laboratory, University of California at Santa Barbara. His area of research is in high-linearity CMOS RF and millimeter-wave circuits.

Dr. Hill serves as a Reviewer for the IEEE TRANSACTIONS ON MICROWAVE THEORY AND TECHNIQUES and IEEE TRANSACTIONS ON CIRCUITS AND SYSTEMS.



**James Buckwalter** (Senior Member, IEEE) received the Ph.D. degree in electrical engineering from the California Institute of Technology, Pasadena, CA, USA, in 2006.

From 1999 to 2000, he was a Research Scientist with Telcordia Technologies, Morristown, NJ, USA. In 2004, he was with the IBM T. J. Watson Research Center, Yorktown Heights, NY, USA. In 2006, he joined the University of California at San Diego, La Jolla, CA, USA, as an Assistant Professor, where he was promoted to Associate Professor in 2012. He is currently a Professor of electrical and computer engineering with the University of California at Santa Barbara, Santa Barbara, CA, USA.

Dr. Buckwalter was a recipient of the 2004 IBM Ph.D. Fellowship, the 2007 Defense Advanced Research Projects Agency Young Faculty Award, the 2011 NSF CAREER Award, and the 2015 IEEE MTT-S Young Engineer Award.